

Study of $D^+ \rightarrow K_S^0 K^*(892)^+$ in $D^+ \rightarrow K_S^0 K_S^0 \pi^+$

M. Ablikim¹, M. N. Achasov^{4,c}, P. Adlarson⁷⁶, O. Afedulidis³, X. C. Ai⁸¹, R. Aliberti³⁵, A. Amoroso^{75A,75C}, Q. An^{72,58,a}, Y. Bai⁵⁷, O. Bakina³⁶, I. Balossino^{29A}, Y. Ban^{46,h}, H.-R. Bao⁶⁴, V. Batzskaya^{1,44}, K. Begzsuren³², N. Berger³⁵, M. Berlowski⁴⁴, M. Bertani^{28A}, D. Bettoni^{29A}, F. Bianchi^{75A,75C}, E. Bianco^{75A,75C}, A. Bortone^{75A,75C}, I. Boyko³⁶, R. A. Briere⁵, A. Brueggemann⁶⁹, H. Cai⁷⁷, X. Cai^{1,58}, A. Calcaterra^{28A}, G. F. Cao^{1,64}, N. Cao^{1,64}, S. A. Cetin^{62A}, J. F. Chang^{1,58}, G. R. Che⁴³, G. Chelkov^{36,b}, C. Chen⁴³, C. H. Chen⁹, Chao Chen⁵⁵, G. Chen¹, H. S. Chen^{1,64}, H. Y. Chen²⁰, M. L. Chen^{1,58,64}, S. J. Chen⁴², S. L. Chen⁴⁵, S. M. Chen⁶¹, T. Chen^{1,64}, X. R. Chen^{31,64}, X. T. Chen^{1,64}, Y. B. Chen^{1,58}, Y. Q. Chen³⁴, Z. J. Chen^{25,i}, Z. Y. Chen^{1,64}, S. K. Choi^{10A}, G. Cibinetto^{29A}, F. Cossio^{75C}, J. J. Cui⁵⁰, H. L. Dai^{1,58}, J. P. Dai⁷⁹, A. Dbeyssi¹⁸, R. E. de Boer³, D. Dedovich³⁶, C. Q. Deng⁷³, Z. Y. Deng¹, A. Denig³⁵, I. Denysenko³⁶, M. Destefanis^{75A,75C}, F. De Mori^{75A,75C}, B. Ding^{67,1}, X. X. Ding^{46,h}, Y. Ding⁴⁰, Y. Ding³⁴, J. Dong^{1,58}, L. Y. Dong^{1,64}, M. Y. Dong^{1,58,64}, X. Dong⁷⁷, M. C. Du¹, S. X. Du⁸¹, Y. Y. Duan⁵⁵, Z. H. Duan⁴², P. Egorov^{36,b}, Y. H. Fan⁴⁵, J. Fang^{1,58}, J. Fang⁵⁹, S. S. Fang^{1,64}, W. X. Fang¹, Y. Fang¹, Y. Q. Fang^{1,58}, R. Farinelli^{29A}, L. Fava^{75B,75C}, F. Feldbauer³, G. Felici^{28A}, C. Q. Feng^{72,58}, J. H. Feng⁵⁹, Y. T. Feng^{72,58}, M. Fritsch³, C. D. Fu¹, J. L. Fu⁶⁴, Y. W. Fu^{1,64}, H. Gao⁶⁴, X. B. Gao⁴¹, Y. N. Gao^{46,h}, Yang Gao^{72,58}, S. Garbolino^{75C}, I. Garzia^{29A,29B}, L. Ge⁸¹, P. T. Ge¹⁹, Z. W. Ge⁴², C. Geng⁵⁹, E. M. Gersabeck⁶⁸, A. Gilman⁷⁰, K. Goetzen¹³, L. Gong⁴⁰, W. X. Gong^{1,58}, W. Gradl³⁵, S. Gramigna^{29A,29B}, M. Greco^{75A,75C}, M. H. Gu^{1,58}, Y. T. Gu¹⁵, C. Y. Guan^{1,64}, A. Q. Guo^{31,64}, L. B. Guo⁴¹, M. J. Guo⁵⁰, R. P. Guo⁴⁹, Y. P. Guo^{12,g}, A. Guskov^{36,b}, J. Gutierrez²⁷, K. L. Han⁶⁴, T. T. Han¹, F. Hanisch³, X. Q. Hao¹⁹, F. A. Harris⁶⁶, K. K. He⁵⁵, K. L. He^{1,64}, F. H. Heinsius³, C. H. Heinz³⁵, Y. K. Heng^{1,58,64}, C. Herold⁶⁰, T. Holtmann³, P. C. Hong³⁴, G. Y. Hou^{1,64}, X. T. Hou^{1,64}, Y. R. Hou⁶⁴, Z. L. Hou¹, B. Y. Hu⁵⁹, H. M. Hu^{1,64}, J. F. Hu^{56,j}, S. L. Hu^{12,g}, T. Hu^{1,58,64}, Y. Hu¹, G. S. Huang^{72,58}, K. X. Huang⁵⁹, L. Q. Huang^{31,64}, X. T. Huang⁵⁰, Y. P. Huang¹, Y. S. Huang⁵⁹, T. Hussain⁷⁴, F. Hölzken³, N. Hüskens³⁵, N. in der Wiesche⁶⁹, J. Jackson²⁷, S. Janchiv³², J. H. Jeong^{10A}, Q. Ji¹, Q. P. Ji¹⁹, W. Ji^{1,64}, X. B. Ji^{1,64}, X. L. Ji^{1,58}, Y. Y. Ji⁵⁰, X. Q. Jia⁵⁰, Z. K. Jia^{72,58}, D. Jiang^{1,64}, H. B. Jiang⁷⁷, P. C. Jiang^{46,h}, S. S. Jiang³⁹, T. J. Jiang¹⁶, X. S. Jiang^{1,58,64}, Y. Q. Jiang⁶⁴, J. B. Jiao⁵⁰, J. K. Jiao³⁴, Z. Jiao²³, S. Jin⁴², Y. Jin⁶⁷, M. Q. Jing^{1,64}, X. M. Jing⁶⁴, T. Johansson⁷⁶, S. Kabana³³, N. Kalantar-Nayestanaki⁶⁵, X. L. Kang⁹, X. S. Kang⁴⁰, M. Kavatsyuk⁶⁵, B. C. Ke⁸¹, V. Khachatryan²⁷, A. Khoukaz⁶⁹, R. Kiuchi¹, O. B. Kolcu^{62A}, B. Kopf³, M. Kuessner³, X. Kui^{1,64}, N. Kumar²⁶, A. Kupsc^{44,76}, W. Kühn³⁷, J. J. Lane⁶⁸, L. Lavezzi^{75A,75C}, T. T. Lei^{72,58}, Z. H. Lei^{72,58}, M. Lellmann³⁵, T. Lenz³⁵, C. Li⁴⁷, C. Li⁴³, C. H. Li³⁹, Cheng Li^{72,58}, D. M. Li⁸¹, F. Li^{1,58}, G. Li¹, H. B. Li^{1,64}, H. J. Li¹⁹, H. N. Li^{56,j}, Hui Li⁴³, J. R. Li⁶¹, J. S. Li⁵⁹, K. Li¹, L. J. Li^{1,64}, L. K. Li¹, Lei Li⁴⁸, M. H. Li⁴³, P. R. Li^{38,k,l}, Q. M. Li^{1,64}, Q. X. Li⁵⁰, R. Li^{17,31}, S. X. Li¹², T. Li⁵⁰, W. D. Li^{1,64}, W. G. Li^{1,a}, X. Li^{1,64}, X. H. Li^{72,58}, X. L. Li⁵⁰, X. Y. Li^{1,64}, X. Z. Li⁵⁹, Y. G. Li^{46,h}, Z. J. Li⁵⁹, Z. Y. Li⁷⁹, C. Liang⁴², H. Liang^{72,58}, H. Liang^{1,64}, Y. F. Liang⁵⁴, Y. T. Liang^{31,64}, G. R. Liao¹⁴, Y. P. Liao^{1,64}, J. Libby²⁶, A. Limphirat⁶⁰, C. C. Lin⁵⁵, D. X. Lin^{31,64}, T. Lin¹, B. J. Liu¹, B. X. Liu⁷⁷, C. Liu³⁴, C. X. Liu¹, F. Liu¹, F. H. Liu⁵³, Feng Liu⁶, G. M. Liu^{56,j}, H. Liu^{38,k,l}, H. B. Liu¹⁵, H. H. Liu¹, H. M. Liu^{1,64}, Huihui Liu²¹, J. B. Liu^{72,58}, J. Y. Liu^{1,64}, K. Liu^{38,k,l}, K. Y. Liu⁴⁰, Ke Liu²², L. Liu^{72,58}, L. C. Liu⁴³, Lu Liu⁴³, M. H. Liu^{12,g}, P. L. Liu¹, Q. Liu⁶⁴, S. B. Liu^{72,58}, T. Liu^{12,g}, W. K. Liu⁴³, W. M. Liu^{72,58}, X. Liu³⁹, X. Liu^{38,k,l}, Y. Liu⁸¹, Y. Liu^{38,k,l}, Y. B. Liu⁴³, Z. A. Liu^{1,58,64}, Z. D. Liu⁹, Z. Q. Liu⁵⁰, X. C. Lou^{1,58,64}, F. X. Lu⁵⁹, H. J. Lu²³, J. G. Lu^{1,58}, X. L. Lu¹, Y. Lu⁷, Y. P. Lu^{1,58}, Z. H. Lu^{1,64}, C. L. Luo⁴¹, J. R. Luo⁵⁹, M. X. Luo⁸⁰, T. Luo^{12,g}, X. L. Luo^{1,58}, X. R. Lyu⁶⁴, Y. F. Lyu⁴³, F. C. Ma⁴⁰, H. Ma⁷⁹, H. L. Ma¹, J. L. Ma^{1,64}, L. L. Ma⁵⁰, L. R. Ma⁶⁷, M. M. Ma^{1,64}, Q. M. Ma¹, R. Q. Ma^{1,64}, T. Ma^{72,58}, X. T. Ma^{1,64}, X. Y. Ma^{1,58}, Y. Ma^{46,h}, Y. M. Ma³¹, F. E. Maas¹⁸, M. Maggiora^{75A,75C}, S. Malde⁷⁰, Y. J. Mao^{46,h}, Z. P. Mao¹, S. Marcello^{75A,75C}, Z. X. Meng⁶⁷, J. G. Messchendorp^{13,65}, G. Mezzadri^{29A}, H. Miao^{1,64}, T. J. Min⁴², R. E. Mitchell²⁷, S. H. Mo^{1,58,64}, B. Moses²⁷, N. Yu. Muchnoi^{4,c}, J. Muskalla³⁵, Y. Nefedov³⁶, F. Nerling^{18,e}, L. S. Nie²⁰, I. B. Nikolaev^{4,c}, Z. Ning^{1,58}, S. Nisar^{11,m}, Q. L. Niu^{38,k,l}, W. D. Niu⁵⁵, Y. Niu⁵⁰, S. L. Olsen⁶⁴, Q. Ouyang^{1,58,64}, S. Pacetti^{28B,28C}, X. Pan⁵⁵, Y. Pan⁵⁷, A. Pathak³⁴, Y. P. Pei^{72,58}, M. Pelizaeus³, H. P. Peng^{72,58}, Y. Y. Peng^{38,k,l}, K. Peters^{13,e}, J. L. Ping⁴¹, R. G. Ping^{1,64}, S. Plura³⁵, V. Prasad³³, F. Z. Qi¹, H. Qi^{72,58}, H. R. Qi⁶¹, M. Qi⁴², T. Y. Qi^{12,g}, S. Qian^{1,58}, W. B. Qian⁶⁴, C. F. Qiao⁶⁴, X. K. Qiao⁸¹, J. J. Qin⁷³, L. Q. Qin¹⁴, L. Y. Qin^{72,58}, X. P. Qin^{12,g}, X. S. Qin⁵⁰, Z. H. Qin^{1,58}, J. F. Qiu¹, Z. H. Qu⁷³, C. F. Redmer³⁵, K. J. Ren³⁹, A. Rivetti^{75C}, M. Rolo^{75C}, G. Rong^{1,64}, Ch. Rosner¹⁸, S. N. Ruan⁴³, N. Salone⁴⁴, A. Sarantsev^{36,d}, Y. Schelhaas³⁵, K. Schoenning⁷⁶, M. Scodreggio^{29A}, K. Y. Shan^{12,g}, W. Shan²⁴, X. Y. Shan^{72,58}, Z. J. Shang^{38,k,l}, J. F. Shangguan¹⁶, L. G. Shao^{1,64}, M. Shao^{72,58}, C. P. Shen^{12,g}, H. F. Shen^{1,8}, W. H. Shen⁶⁴, X. Y. Shen^{1,64}, B. A. Shi⁶⁴, H. Shi^{72,58}, H. C. Shi^{72,58}, J. L. Shi^{12,g}, J. Y. Shi¹, Q. Q. Shi⁵⁵, S. Y. Shi⁷³, X. Shi^{1,58}, J. J. Song¹⁹, T. Z. Song⁵⁹, W. M. Song^{34,1}, Y. J. Song^{12,g}, Y. X. Song^{46,h,n}, S. Sosio^{75A,75C}, S. Spataro^{75A,75C}, F. Stieler³⁵, Y. J. Su⁶⁴, G. B. Sun⁷⁷, G. X. Sun¹, H. Sun⁶⁴, H. K. Sun¹, J. F. Sun¹⁹, K. Sun⁶¹, L. Sun⁷⁷, S. S. Sun^{1,64}, T. Sun^{51,f}, W. Y. Sun³⁴, Y. Sun⁹, Y. J. Sun^{72,58}, Y. Z. Sun¹, Z. Q. Sun^{1,64}, Z. T. Sun⁵⁰, C. J. Tang⁵⁴, G. Y. Tang¹, J. Tang⁵⁹, M. Tang^{72,58}, Y. A. Tang⁷⁷, L. Y. Tao⁷³, Q. T. Tao^{25,i}, M. Tat⁷⁰, J. X. Teng^{72,58}, V. Thoren⁷⁶, W. H. Tian⁵⁹, Y. Tian^{31,64}, Z. F. Tian⁷⁷, I. Uman^{62B}, Y. Wan⁵⁵, S. J. Wang⁵⁰, B. Wang¹, B. L. Wang⁶⁴, Bo Wang^{72,58}, D. Y. Wang^{46,h}, F. Wang⁷³, H. J. Wang^{38,k,l}, J. J. Wang⁷⁷, J. P. Wang⁵⁰, K. Wang^{1,58}, L. L. Wang¹, M. Wang⁵⁰, N. Y. Wang⁶⁴, S. Wang^{12,g}, S. Wang^{38,k,l}, T. Wang^{12,g}, T. J. Wang⁴³, W. Wang⁷³, W. Wang⁵⁹, W. P. Wang^{35,72,o}, W. P. Wang^{72,58}, X. Wang^{46,h}, X. F. Wang^{38,k,l}, X. J. Wang³⁹, X. L. Wang^{12,g}, X. N. Wang¹, Y. Wang⁶¹, Y. D. Wang⁴⁵, Y. F. Wang^{1,58,64}, Y. L. Wang¹⁹, Y. N. Wang⁴⁵, Y. Q. Wang¹, Yaqian Wang¹⁷, Yi Wang⁶¹, Z. Wang^{1,58}, Z. L. Wang⁷³, Z. Y. Wang^{1,64}, Ziyi Wang⁶⁴, D. H. Wei¹⁴, F. Weidner⁶⁹, S. P. Wen¹, Y. R. Wen³⁹, U. Wiedner³, G. Wilkinson⁷⁰, M. Wolke⁷⁶, L. Wollenberg³, C. Wu³⁹, J. F. Wu^{1,8}, L. H. Wu¹, L. J. Wu^{1,64}, X. Wu^{12,g}, X. H. Wu³⁴, Y. Wu^{72,58}, Y. H. Wu⁵⁵, Y. J. Wu³¹, Z. Wu^{1,58}, L. Xia^{72,58}, X. M. Xian³⁹, B. H. Xiang^{1,64}, T. Xiang^{46,h}, D. Xiao^{38,k,l}, G. Y. Xiao⁴², S. Y. Xiao¹, Y. L. Xiao^{12,g}, Z. J. Xiao⁴¹, C. Xie⁴², X. H. Xie^{46,h}, Y. Xie⁵⁰, Y. G. Xie^{1,58}, Y. H. Xie⁶, Z. P. Xie^{72,58}, T. Y. Xing^{1,64}, C. F. Xu^{1,64}, C. J. Xu⁵⁹, G. F. Xu¹, H. Y. Xu^{67,2,p}, M. Xu^{72,58}, Q. J. Xu¹⁶, Q. N. Xu³⁰, W. Xu¹, W. L. Xu⁶⁷, X. P. Xu⁵⁵, Y. C. Xu⁷⁸, Z. S. Xu⁶⁴, F. Yan^{12,g}, L. Yan^{12,g}, W. B. Yan^{72,58}, W. C. Yan⁸¹

X. Q. Yan^{1,64}, H. J. Yang^{51,f}, H. L. Yang³⁴, H. X. Yang¹, T. Yang¹, Y. Yang^{12,g}, Y. F. Yang^{1,64}, Y. F. Yang⁴³,
 Y. X. Yang^{1,64}, Z. W. Yang^{38,k,l}, Z. P. Yao⁵⁰, M. Ye^{1,58}, M. H. Ye⁸, J. H. Yin¹, Junhao Yin⁴³, Z. Y. You⁵⁹, B. X. Yu^{1,58,64},
 C. X. Yu⁴³, G. Yu^{1,64}, J. S. Yu^{25,i}, T. Yu⁷³, X. D. Yu^{46,h}, Y. C. Yu⁸¹, C. Z. Yuan^{1,64}, J. Yuan⁴⁵, J. Yuan³⁴, L. Yuan²,
 S. C. Yuan^{1,64}, Y. Yuan^{1,64}, Z. Y. Yuan⁵⁹, C. X. Yue³⁹, A. A. Zafar⁷⁴, F. R. Zeng⁵⁰, S. H. Zeng^{63A,63B,63C,63D}, X. Zeng^{12,g},
 Y. Zeng^{25,i}, Y. J. Zeng⁵⁹, Y. J. Zeng^{1,64}, X. Y. Zhai³⁴, Y. C. Zhai⁵⁰, Y. H. Zhan⁵⁹, A. Q. Zhang^{1,64}, B. L. Zhang^{1,64},
 B. X. Zhang¹, D. H. Zhang⁴³, G. Y. Zhang¹⁹, H. Zhang⁸¹, H. Zhang^{72,58}, H. C. Zhang^{1,58,64}, H. H. Zhang⁵⁹, H. H. Zhang³⁴,
 H. Q. Zhang^{1,58,64}, H. R. Zhang^{72,58}, H. Y. Zhang^{1,58}, J. Zhang⁸¹, J. Zhang⁵⁹, J. J. Zhang⁵², J. L. Zhang²⁰, J. Q. Zhang⁴¹,
 J. S. Zhang^{12,g}, J. W. Zhang^{1,58,64}, J. X. Zhang^{38,k,l}, J. Y. Zhang¹, J. Z. Zhang^{1,64}, Jianyu Zhang⁶⁴, L. M. Zhang⁶¹,
 Lei Zhang⁴², P. Zhang^{1,64}, Q. Y. Zhang³⁴, R. Y. Zhang^{38,k,l}, S. H. Zhang^{1,64}, Shulei Zhang^{25,i}, X. D. Zhang⁴⁵, X. M. Zhang¹,
 X. Y. Zhang⁵⁰, Y. Zhang⁷³, Y. Zhang¹, Y. T. Zhang⁸¹, Y. H. Zhang^{1,58}, Y. M. Zhang³⁹, Yan Zhang^{72,58}, Z. D. Zhang¹,
 Z. H. Zhang¹, Z. L. Zhang³⁴, Z. Y. Zhang⁴³, Z. Y. Zhang⁷⁷, Z. Z. Zhang⁴⁵, G. Zhao¹, J. Y. Zhao^{1,64}, J. Z. Zhao^{1,58},
 L. Zhao¹, Lei Zhao^{72,58}, M. G. Zhao⁴³, N. Zhao⁷⁹, R. P. Zhao⁶⁴, S. J. Zhao⁸¹, Y. B. Zhao^{1,58}, Y. X. Zhao^{31,64},
 Z. G. Zhao^{72,58}, A. Zhemchugov^{36,b}, B. Zheng⁷³, B. M. Zheng³⁴, J. P. Zheng^{1,58}, W. J. Zheng^{1,64}, Y. H. Zheng⁶⁴, B. Zhong⁴¹,
 X. Zhong⁵⁹, H. Zhou⁵⁰, J. Y. Zhou³⁴, L. P. Zhou^{1,64}, S. Zhou⁶, X. Zhou⁷⁷, X. K. Zhou⁶, X. R. Zhou^{72,58}, X. Y. Zhou³⁹,
 Y. Z. Zhou^{12,g}, A. N. Zhu⁶⁴, J. Zhu⁴³, K. Zhu¹, K. J. Zhu^{1,58,64}, K. S. Zhu^{12,g}, L. Zhu³⁴, L. X. Zhu⁶⁴, S. H. Zhu⁷¹,
 T. J. Zhu^{12,g}, W. D. Zhu⁴¹, Y. C. Zhu^{72,58}, Z. A. Zhu^{1,64}, J. H. Zou¹, J. Zu^{72,58}

(BESIII Collaboration)

¹ Institute of High Energy Physics, Beijing 100049, People's Republic of China

² Beihang University, Beijing 100191, People's Republic of China

³ Bochum Ruhr-University, D-44780 Bochum, Germany

⁴ Budker Institute of Nuclear Physics SB RAS (BINP), Novosibirsk 630090, Russia

⁵ Carnegie Mellon University, Pittsburgh, Pennsylvania 15213, USA

⁶ Central China Normal University, Wuhan 430079, People's Republic of China

⁷ Central South University, Changsha 410083, People's Republic of China

⁸ China Center of Advanced Science and Technology, Beijing 100190, People's Republic of China

⁹ China University of Geosciences, Wuhan 430074, People's Republic of China

¹⁰ Chung-Ang University, Seoul, 06974, Republic of Korea

¹¹ COMSATS University Islamabad, Lahore Campus, Defence Road, Off Raiwind Road, 54000 Lahore, Pakistan

¹² Fudan University, Shanghai 200433, People's Republic of China

¹³ GSI Helmholtzcentre for Heavy Ion Research GmbH, D-64291 Darmstadt, Germany

¹⁴ Guangxi Normal University, Guilin 541004, People's Republic of China

¹⁵ Guangxi University, Nanning 530004, People's Republic of China

¹⁶ Hangzhou Normal University, Hangzhou 310036, People's Republic of China

¹⁷ Hebei University, Baoding 071002, People's Republic of China

¹⁸ Helmholtz Institute Mainz, Staudinger Weg 18, D-55099 Mainz, Germany

¹⁹ Henan Normal University, Xinxiang 453007, People's Republic of China

²⁰ Henan University, Kaifeng 475004, People's Republic of China

²¹ Henan University of Science and Technology, Luoyang 471003, People's Republic of China

²² Henan University of Technology, Zhengzhou 450001, People's Republic of China

²³ Huangshan College, Huangshan 245000, People's Republic of China

²⁴ Hunan Normal University, Changsha 410081, People's Republic of China

²⁵ Hunan University, Changsha 410082, People's Republic of China

²⁶ Indian Institute of Technology Madras, Chennai 600036, India

²⁷ Indiana University, Bloomington, Indiana 47405, USA

²⁸ INFN Laboratori Nazionali di Frascati, (A)INFN Laboratori Nazionali di Frascati, I-00044, Frascati, Italy; (B)INFN

Sezione di Perugia, I-06100, Perugia, Italy; (C)University of Perugia, I-06100, Perugia, Italy

²⁹ INFN Sezione di Ferrara, (A)INFN Sezione di Ferrara, I-44122, Ferrara, Italy; (B)University of Ferrara, I-44122, Ferrara, Italy

³⁰ Inner Mongolia University, Hohhot 010021, People's Republic of China

³¹ Institute of Modern Physics, Lanzhou 730000, People's Republic of China

³² Institute of Physics and Technology, Peace Avenue 54B, Ulaanbaatar 13330, Mongolia

³³ Instituto de Alta Investigación, Universidad de Tarapacá, Casilla 7D, Arica 1000000, Chile

³⁴ Jilin University, Changchun 130012, People's Republic of China

³⁵ Johannes Gutenberg University of Mainz, Johann-Joachim-Becher-Weg 45, D-55099 Mainz, Germany

³⁶ Joint Institute for Nuclear Research, 141980 Dubna, Moscow region, Russia

³⁷ Justus-Liebig-Universität Giessen, II. Physikalisches Institut, Heinrich-Buff-Ring 16, D-35392 Giessen, Germany

³⁸ Lanzhou University, Lanzhou 730000, People's Republic of China

³⁹ Liaoning Normal University, Dalian 116029, People's Republic of China

⁴⁰ Liaoning University, Shenyang 110036, People's Republic of China

⁴¹ Nanjing Normal University, Nanjing 210023, People's Republic of China

⁴² Nanjing University, Nanjing 210093, People's Republic of China

⁴³ Nankai University, Tianjin 300071, People's Republic of China

- ⁴⁴ National Centre for Nuclear Research, Warsaw 02-093, Poland
- ⁴⁵ North China Electric Power University, Beijing 102206, People's Republic of China
- ⁴⁶ Peking University, Beijing 100871, People's Republic of China
- ⁴⁷ Qufu Normal University, Qufu 273165, People's Republic of China
- ⁴⁸ Renmin University of China, Beijing 100872, People's Republic of China
- ⁴⁹ Shandong Normal University, Jinan 250014, People's Republic of China
- ⁵⁰ Shandong University, Jinan 250100, People's Republic of China
- ⁵¹ Shanghai Jiao Tong University, Shanghai 200240, People's Republic of China
- ⁵² Shanxi Normal University, Linfen 041004, People's Republic of China
- ⁵³ Shanxi University, Taiyuan 030006, People's Republic of China
- ⁵⁴ Sichuan University, Chengdu 610064, People's Republic of China
- ⁵⁵ Soochow University, Suzhou 215006, People's Republic of China
- ⁵⁶ South China Normal University, Guangzhou 510006, People's Republic of China
- ⁵⁷ Southeast University, Nanjing 211100, People's Republic of China
- ⁵⁸ State Key Laboratory of Particle Detection and Electronics, Beijing 100049, Hefei 230026, People's Republic of China
- ⁵⁹ Sun Yat-Sen University, Guangzhou 510275, People's Republic of China
- ⁶⁰ Suranaree University of Technology, University Avenue 111, Nakhon Ratchasima 30000, Thailand
- ⁶¹ Tsinghua University, Beijing 100084, People's Republic of China
- ⁶² Turkish Accelerator Center Particle Factory Group, (A)Istinye University, 34010, Istanbul, Turkey; (B)Near East University, Nicosia, North Cyprus, 99138, Mersin 10, Turkey
- ⁶³ University of Bristol, (A)H H Wills Physics Laboratory; (B)Tyndall Avenue; (C)Bristol; (D)BS8 1TL
- ⁶⁴ University of Chinese Academy of Sciences, Beijing 100049, People's Republic of China
- ⁶⁵ University of Groningen, NL-9747 AA Groningen, The Netherlands
- ⁶⁶ University of Hawaii, Honolulu, Hawaii 96822, USA
- ⁶⁷ University of Jinan, Jinan 250022, People's Republic of China
- ⁶⁸ University of Manchester, Oxford Road, Manchester, M13 9PL, United Kingdom
- ⁶⁹ University of Muenster, Wilhelm-Klemm-Strasse 9, 48149 Muenster, Germany
- ⁷⁰ University of Oxford, Keble Road, Oxford OX13RH, United Kingdom
- ⁷¹ University of Science and Technology Liaoning, Anshan 114051, People's Republic of China
- ⁷² University of Science and Technology of China, Hefei 230026, People's Republic of China
- ⁷³ University of South China, Hengyang 421001, People's Republic of China
- ⁷⁴ University of the Punjab, Lahore-54590, Pakistan
- ⁷⁵ University of Turin and INFN, (A)University of Turin, I-10125, Turin, Italy; (B)University of Eastern Piedmont, I-15121, Alessandria, Italy; (C)INFN, I-10125, Turin, Italy
- ⁷⁶ Uppsala University, Box 516, SE-75120 Uppsala, Sweden
- ⁷⁷ Wuhan University, Wuhan 430072, People's Republic of China
- ⁷⁸ Yantai University, Yantai 264005, People's Republic of China
- ⁷⁹ Yunnan University, Kunming 650500, People's Republic of China
- ⁸⁰ Zhejiang University, Hangzhou 310027, People's Republic of China
- ⁸¹ Zhengzhou University, Zhengzhou 450001, People's Republic of China
- ^a Deceased
- ^b Also at the Moscow Institute of Physics and Technology, Moscow 141700, Russia
- ^c Also at the Novosibirsk State University, Novosibirsk, 630090, Russia
- ^d Also at the NRC "Kurchatov Institute", PNPI, 188300, Gatchina, Russia
- ^e Also at Goethe University Frankfurt, 60323 Frankfurt am Main, Germany
- ^f Also at Key Laboratory for Particle Physics, Astrophysics and Cosmology, Ministry of Education; Shanghai Key Laboratory for Particle Physics and Cosmology; Institute of Nuclear and Particle Physics, Shanghai 200240, People's Republic of China
- ^g Also at Key Laboratory of Nuclear Physics and Ion-beam Application (MOE) and Institute of Modern Physics, Fudan University, Shanghai 200443, People's Republic of China
- ^h Also at State Key Laboratory of Nuclear Physics and Technology, Peking University, Beijing 100871, People's Republic of China
- ⁱ Also at School of Physics and Electronics, Hunan University, Changsha 410082, China
- ^j Also at Guangdong Provincial Key Laboratory of Nuclear Science, Institute of Quantum Matter, South China Normal University, Guangzhou 510006, China
- ^k Also at MOE Frontiers Science Center for Rare Isotopes, Lanzhou University, Lanzhou 730000, People's Republic of China
- ^l Also at Lanzhou Center for Theoretical Physics, Lanzhou University, Lanzhou 730000, People's Republic of China
- ^m Also at the Department of Mathematical Sciences, IBA, Karachi 75270, Pakistan
- ⁿ Also at Ecole Polytechnique Federale de Lausanne (EPFL), CH-1015 Lausanne, Switzerland
- ^o Also at Helmholtz Institute Mainz, Staudinger Weg 18, D-55099 Mainz, Germany
- ^p Also at School of Physics, Beihang University, Beijing 100191, China

(Dated: September 4, 2024)

Using a data sample of e^+e^- collisions corresponding to an integrated luminosity of 7.93 fb^{-1} collected with the BESIII detector at the center-of-mass energy 3.773 GeV , we perform the first amplitude analysis of the decay $D^+ \rightarrow K_S^0 K_S^0 \pi^+$. The absolute branching fraction of $D^+ \rightarrow K_S^0 K_S^0 \pi^+$ is measured to be $(2.97 \pm 0.09_{\text{stat.}} \pm 0.05_{\text{syst.}}) \times 10^{-3}$. The dominant intermediate process is $D^+ \rightarrow K_S^0 K^*(892)^+$, whose branching fraction is determined to be $(8.72 \pm 0.28_{\text{stat.}} \pm 0.15_{\text{syst.}}) \times 10^{-3}$, including all the $K^*(892)^+$ decays.

I. INTRODUCTION

The masses of the charmed mesons, approximately $2 \text{ GeV}/c^2$, fall within a region where non-perturbative Quantum Chromodynamics (QCD) is no longer negligible. This presents a challenge for studying the hadronic transitions of charmed meson. The lightest charmed mesons $D^{0(+)}$ can only decay through weak interactions, and the related amplitudes are dominated by two-body processes, i.e. $D \rightarrow VP$, $D \rightarrow PP$, $D \rightarrow SP$ and $D \rightarrow VV$ decays, where V , S , and P denote vector, scalar and pseudoscalar mesons, respectively. In particular, the $D \rightarrow VP$ decays offer cleaner opportunities than other two-body processes for clarifying the nonperturbative mechanism of charmed meson decays [1–3]. Compared to the $D \rightarrow SP$ decay, the VP system presents a more well-defined quark content of the vector meson than that of the scalar state, whose quark content is still a matter of controversy and is further complicated by significant long-distance rescattering effects [4–6]. The VP system also can be more favorably described by the theoretical framework than the PP and VV systems, due to the multiple-amplitude composition of some P states [2, 3] and the polarization in VV systems [7].

While most of the theoretical predicted branching fractions (BFs) of $D \rightarrow VP$ decays are consistent with experimental measurements, that for $D^+ \rightarrow K_S^0 K^*(892)^+$ shows inconsistency. The $D^+ \rightarrow K_S^0 K^*(892)^+$ decay is one of the most important singly-Cabbibo-suppressed (SCS) $D \rightarrow VP$ decays [8, 9], which can be mediated via color-favored, W -annihilation, and penguin diagrams [2] as shown in Fig. 1. The predicted and measured values of the BF $\mathcal{B}(D^+ \rightarrow K_S^0 K^*(892)^+)$ are listed in Table I, where predicted BFs of the decay $D^+ \rightarrow K_S^0 K^*(892)^+$ are from the pole model [10], the factorization-assisted topological-amplitude (FAT [mix]) approach with $\rho - \omega$ mixing [11], the topological diagram approach (TDA) with only tree level amplitude (denoted as TDA [tree]) [1], including QCD-penguin amplitudes (denoted as TDA [QCD-penguin]) [2] and the updated analysis of the two-body $D \rightarrow VP$ decays within the framework of the TDA [12].

An amplitude analysis of decays with multi-body final states is performed to extract the information of sub-process via intermediate resonance. The BESIII collaboration has measured the BF of $D^+ \rightarrow K_S^0 K^*(892)^+$ to be $(8.69 \pm 0.40_{\text{stat.}} \pm 0.64_{\text{syst.}} \pm 0.51_{\text{Br.}}) \times 10^{-3}$ in the amplitude analysis of $D^+ \rightarrow K^+ K_S^0 \pi^0$ [9] using a

data sample corresponding to an integrated luminosity of 2.93 fb^{-1} at the center-of-mass energy 3.773 GeV , where the third uncertainty is due to the quoted uncertainty of $\mathcal{B}(D^+ \rightarrow K^+ K_S^0 \pi^0)$ [8]. This result differs from the theoretical predictions in Refs. [1, 2, 11] by about 4σ . Therefore, a more precise measurement of $D^+ \rightarrow K_S^0 K^*(892)^+$ is needed to provide a more stringent test of the models and to deepen our understanding of the dynamics of charmed meson decays. A clearer environment is expected to be offered in the $D^+ \rightarrow K_S^0 K_S^0 \pi^+$ decay without the interference from $D^+ \rightarrow K^+ K^*(892)^0$ in $D^+ \rightarrow K^+ K_S^0 \pi^0$.

The $D^+ \rightarrow K_S^0 K_S^0 \pi^+$ decay has been previously observed by the BESIII collaboration with a BF of $\mathcal{B}(D^+ \rightarrow K_S^0 K_S^0 \pi^+) = (2.70 \pm 0.05_{\text{stat.}} \pm 0.12_{\text{syst.}}) \times 10^{-3}$ [13]. Using a data sample of e^+e^- collisions corresponding to an integrated luminosity of 7.93 fb^{-1} [14] collected by the BESIII detector [15] at the center-of-mass energy 3.773 GeV , we performed the first amplitude analysis and the absolute BF measurement of the SCS decay $D^+ \rightarrow K_S^0 K_S^0 \pi^+$. Charge-conjugate states are implied throughout this paper, allowing for the signal-side decay $D^- \rightarrow K_S^0 K_S^0 \pi^-$.

TABLE I. Theoretical predictions of $\mathcal{B}(D^+ \rightarrow K_S^0 K^*(892)^+)$ and the previous experimental measurement.

Model	$\mathcal{B}(D^+ \rightarrow K_S^0 K^*(892)^+) (\times 10^{-3})$
Pole [10]	6.2 ± 1.2
FAT [mix] [11]	5.5
TDA [tree] [1]	5.02 ± 1.31
TDA [QCD-penguin] [2]	4.90 ± 0.21
TDA [12]	7.90 ± 0.25
BESIII measurement [9]	$8.69 \pm 0.40_{\text{stat.}} \pm 0.64_{\text{syst.}} \pm 0.51_{\text{BF}}$

II. DETECTOR AND MONTE CARLO SIMULATION

The BESIII detector [15] records symmetric e^+e^- collisions provided by the BEPCII storage ring [16] in the center-of-mass energy range from 2.00 to 4.95 GeV , with a peak luminosity of $1 \times 10^{33} \text{ cm}^{-2}\text{s}^{-1}$ achieved at $\sqrt{s} = 3.77 \text{ GeV}$. BESIII has collected large data samples in this energy region [17–19]. The cylindrical core of the BESIII detector covers 93% of the full solid angle and consists of a helium-based multilayer drift chamber (MDC),

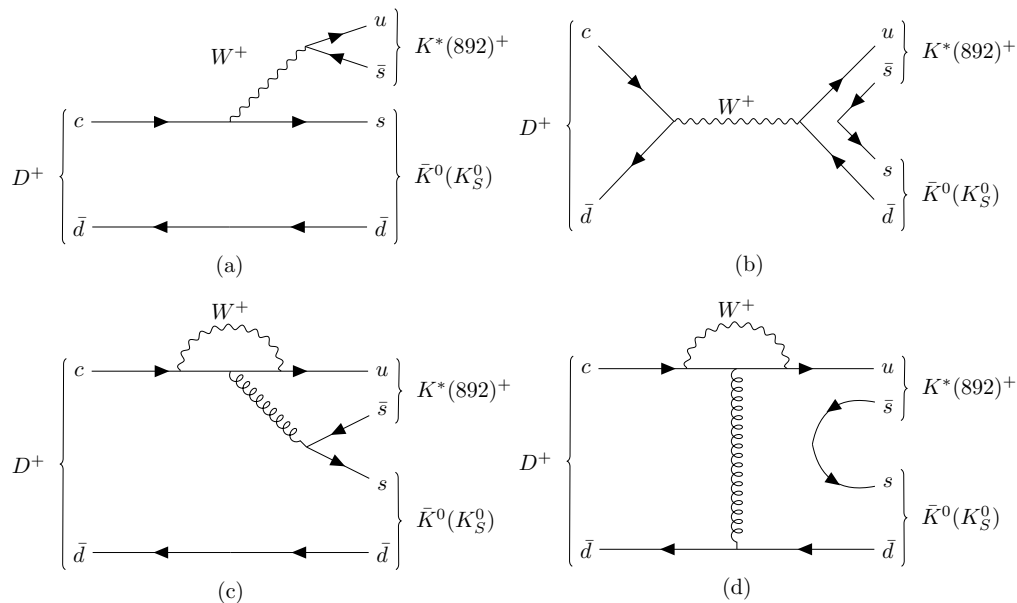


FIG. 1. Topological diagrams contributing to the decay $D^+ \rightarrow K_S^0 K^*(892)^+$ with (a) color allowed external W -emission tree diagram, (b) W -annihilation diagram, (c) color suppressed external W -emission QCD-penguin diagram and (d) QCD-penguin exchange diagram.

a plastic scintillator time-of-flight system (TOF), and a CsI(Tl) electromagnetic calorimeter (EMC), which are all enclosed in a superconducting solenoidal magnet providing a 1.0 T magnetic field. The solenoid is supported by an octagonal flux-return yoke with resistive plate counter muon identification modules interleaved with steel. The charged-particle momentum resolution at 1 GeV/ c is 0.5%, and the dE/dx resolution is 6% for electrons from Bhabha scattering. The EMC measures photon energies with a resolution of 2.5% (5%) at 1 GeV in the barrel (end cap) region. The time resolution in the TOF barrel region is 68 ps, while that in the end cap region was 110 ps. The end cap TOF system was upgraded in 2015 using multigap resistive plate chamber technology, providing a time resolution of 60 ps, which benefits 63% of the data used in this analysis [20].

Simulated inclusive Monte Carlo (MC) samples are produced with a GEANT4-based [21] MC simulation package, which includes the geometric description of the BESIII detector [22] and the detector response, and are used to determine detection efficiencies and to estimate backgrounds. The simulation models the beam energy spread and initial state radiation (ISR) in the e^+e^- annihilations with the generator KKMC [23]. The inclusive MC samples consist of the production of $D\bar{D}$ pairs, the non- $D\bar{D}$ decays of the $\psi(3770)$, the ISR production of the J/ψ and $\psi(3686)$ states, and the continuum processes incorporated in KKMC. All particle decays are modelled with EVTGEN [24] using BF's either taken from the Particle Data Group (PDG) [25], when available, or otherwise estimated with LUNDCHARM [26]. Final state radiation

from charged final state particles is incorporated using PHOTOS [27]. In this work, two sets of MC samples are used. The phase space (PHSP) MC sample is generated with a uniform distribution in phase space for the decay $D^+ \rightarrow K_S^0 K_S^0 \pi^+$, which is used to calculate the normalization factor of the probability density function (PDF) in the amplitude analysis. The signal MC sample, which is used to estimate the detection efficiencies, is generated according to the amplitude analysis results.

III. EVENT SELECTION

The process $e^+e^- \rightarrow \psi(3770) \rightarrow D^+D^-$ allows studies of D decays with a tag technique [28, 29]. There are two types of samples used with the tag technique: single tag (ST) and double tag (DT). In the ST sample, only one D^- meson is reconstructed through one of six hadronic decay modes: $D^- \rightarrow K^+\pi^-\pi^-$, $K^+\pi^-\pi^-\pi^0$, $K_S^0\pi^-$, $K_S^0\pi^-\pi^0$, $K_S^0\pi^-\pi^-\pi^+$, and $K^+K^-\pi^-$. In the DT sample, the signal D^+ is reconstructed through $D^+ \rightarrow K_S^0 K_S^0 \pi^+$.

All charged tracks detected in the MDC must satisfy $|\cos\theta| < 0.93$, where θ is defined as the polar angle with respect to the z -axis, which is the symmetry axis of the MDC. For charged tracks not originating from K_S^0 decays, the distance of closest approach to the interaction point (IP) is required to be less than 1 cm in the transverse plane ($|V_{xy}|$), and less than 10 cm along the z -axis ($|V_z|$). Particle identification (PID) for charged tracks combines the dE/dx measurement in the MDC with the

time of flight measurement of the TOF detector to define the likelihood function $\mathcal{L}(h)$ ($h = K, \pi$) for each hadron (h) hypothesis. The charged kaons and pions are identified by comparing the likelihoods for the kaon and pion hypotheses, $\mathcal{L}(K) > \mathcal{L}(\pi)$ and $\mathcal{L}(\pi) > \mathcal{L}(K)$, respectively.

Each K_S^0 candidate is reconstructed from two oppositely charged tracks satisfying $|V_z| < 20$ cm. The two charged tracks are assigned as $\pi^+\pi^-$ without imposing PID. They are constrained to originate from a common vertex and are required to have an invariant mass $M_{\pi^+\pi^-}$ such that $|M_{\pi^+\pi^-} - m_{K_S^0}| < 12$ MeV/ c^2 , where $m_{K_S^0}$ is the known K^0 mass [25]. The decay length of the K_S^0 candidate is required to be greater than twice its resolution.

Photon candidates are selected using EMC showers. The deposited energy of each shower in the barrel region ($|\cos\theta| < 0.80$) and in the end-cap region ($0.86 < |\cos\theta| < 0.92$) must be greater than 25 MeV and 50 MeV, respectively. To exclude showers that originate from charged tracks, the angle subtended by the EMC shower and the position of the closest charged track at the EMC must be greater than 10 degrees as measured from the IP. The difference between the EMC time and the event start time is required to be within $[0, 700]$ ns to suppress electronic noise and showers unrelated to the event.

The π^0 candidates are reconstructed from photon pairs with invariant masses in the range $[0.115, 0.150]$ GeV/ c^2 , which corresponds to about three times the invariant mass resolution. We require that at least one photon comes from the barrel region of the EMC to improve the resolution. Furthermore, the π^0 candidates are constrained to the known π^0 mass [25] via a kinematic fit to improve their energy and momentum resolution.

Two variables, the beam-constrained mass M_{BC} and the energy difference ΔE , are used to identify the D^+ mesons:

$$\begin{aligned} M_{\text{BC}} &= \sqrt{E_{\text{beam}}^2/c^4 - |\vec{p}_{D^+}|^2/c^2}, \\ \Delta E &= E_{D^+} - E_{\text{beam}}, \end{aligned} \quad (1)$$

where E_{beam} is the beam energy, and \vec{p}_{D^+} and E_{D^+} are the total reconstructed momentum and energy of the D^+ candidate in the e^+e^- rest frame, respectively. The D^+ signals appear as a peak at the known D^+ mass [25] in the M_{BC} distribution and as a peak at zero in the ΔE distribution. The selection criteria of K_S^0 and π^+ on the signal side are the same as those on the tag side. If multiple DT candidates exist in one event, the candidate with the minimum $|\Delta E_{\text{sig}}|$ from the D^+ mesons is retained.

TABLE II. Requirements of ΔE_{tag} for different D^- tag modes.

D^- decay	ΔE_{tag} (GeV)
$K^+\pi^-\pi^-$	$(-0.025, 0.024)$
$K^+\pi^-\pi^-\pi^0$	$(-0.057, 0.046)$
$K_S^0\pi^-$	$(-0.025, 0.026)$
$K_S^0\pi^-\pi^0$	$(-0.062, 0.049)$
$K_S^0\pi^-\pi^-\pi^+$	$(-0.028, 0.027)$
$K^+K^-\pi^-$	$(-0.024, 0.023)$

IV. BACKGROUND STUDY

To increase the signal purity for amplitude analysis, we require $1.863 < M_{\text{BC}} < 1.877$ GeV/ c^2 for all tag modes, and $1.865 < M_{\text{BC}} < 1.875$ GeV/ c^2 and $-0.020 < \Delta E < 0.020$ GeV for the signal side. The boundaries of ΔE_{tag} requirements are listed in Table II. Then, we study the sources of background for $D^+ \rightarrow K_S^0 K_S^0 \pi^+$ by analyzing the inclusive MC samples. The main background is the decay $D^+ \rightarrow K_S^0 \pi^+ \pi^- \pi^+$, since the combinatorial $\pi^+\pi^-$ pairs may accidentally satisfy the K_S^0 selection criteria and contribute as a peak around the D^+ mass in the M_{BC} distribution. This peaking background is estimated with events in the K_S^0 sideband region, defined as $0.020 < |M_{\pi^+\pi^-} - m_{K_S^0}| < 0.044$ GeV/ c^2 . The two dimensional (2D) K_S^0 signal region is defined as the square region with both $\pi^+\pi^-$ combinations lying in the 1D K_S^0 signal region. The 2D K_S^0 sideband 1 (2) regions are defined as the square regions with 1 (2) $\pi^+\pi^-$ combination(s) located in the 1D K_S^0 sideband regions and the rest in the 1D K_S^0 signal region. Figure 2 shows the 2D distribution of $M_{\pi^+\pi^-(1)}$ versus $M_{\pi^+\pi^-(2)}$ for the $D^+ \rightarrow K_S^0 K_S^0 \pi^+$ candidates in data, where the two K_S^0 candidates are randomized.

In this analysis, the combinatorial background in the $M_{\pi^+\pi^-}$ distribution is assumed to be flat, and the net number of $D^+ \rightarrow K_S^0 K_S^0 \pi^+$ signal events is estimated as:

$$N_{\text{net}} = N_{K_S^0 \text{sig}} - \frac{1}{2} N_{\text{sb1}} + \frac{1}{4} N_{\text{sb2}}, \quad (2)$$

where $N_{K_S^0 \text{sig}}$, N_{sb1} and N_{sb2} are the numbers of D^+ meson in the signal, the sideband 1 and the sideband 2 regions, respectively, from fitting the M_{BC} distributions of the accepted candidate events as explained in the next paragraph. The resulting M_{BC} distributions are shown in Fig. 3, and the measured value of N_{net} is given in Table III.

There are 1177 DT events obtained for the amplitude analysis with a signal purity of $(89.1 \pm 2.9)\%$, which is determined from a 2D unbinned maximum likelihood fit to the M_{BC} of the tag D^- versus the M_{BC} of the signal candidates. Figure 4 shows the $M_{\text{BC}}^{\text{tag}}$ versus $M_{\text{BC}}^{\text{sig}}$ distribution for the $D^+ \rightarrow K_S^0 K_S^0 \pi^+$ candidate events

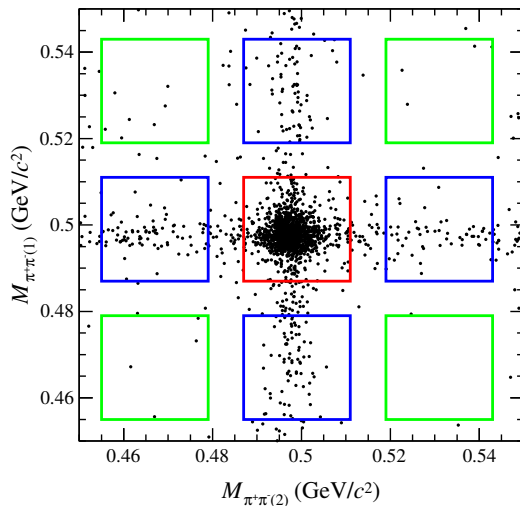


FIG. 2. Distribution of $M_{\pi+\pi-(1)}$ versus $M_{\pi+\pi-(2)}$ for the $D^+ \rightarrow K_S^0 K_S^0 \pi^+$ candidate events in data. The red solid box denotes the 2D signal region. The blue (green) solid boxes indicate the 2D sideband 1 (2) regions.

in data. The signal events with both the tag and the signal side correctly reconstructed concentrate around $M_{\text{BC}}^{\text{sig}} = M_{\text{BC}}^{\text{tag}} = m_{D^+}$, where m_{D^+} is the known D^+ mass. The resolution of the signal peak is primarily influenced by the momentum resolution of the detector and the beam energy spread. The $D^{+(-)}$ momentum resolution $\sigma(D^{+(-)})$ causes the signal peak to be smeared along the $M_{\text{BC}}^{\text{sig}}$ ($M_{\text{BC}}^{\text{tag}}$) axis, while the beam energy spread $\sigma(E_{\text{beam}})$ blurs the signal peak along the diagonal axis, $M_{\text{BC}}^{\text{sig}} + M_{\text{BC}}^{\text{tag}}$, due to its correlation with the $M_{\text{BC}}^{\text{sig}}$ and $M_{\text{BC}}^{\text{tag}}$ variables. Additionally, the signal peak is influenced by the ISR process, which makes the available E_{beam} smaller than the effective beam energy, leading to a diagonal ISR tail oriented toward the high diagonal axis. Besides signal events, we define three kinds of background. Candidates with correctly reconstructed D^+ (or D^-) and incorrectly reconstructed D^- (or D^+) are denoted as BG-I, which appear around the lines $M_{\text{BC}}^{\text{sig}}$ or $M_{\text{BC}}^{\text{tag}} = m_{D^+}$. Other candidates appearing along the diagonal (mispertitioning continuum) arise from decay modes sharing the same final state particle combination with the signal (BG-II). In these cases, one or more particles are associated to the wrong D meson, assuming all final state particles are well-reconstructed. Consequently, the momentum of each signal or tag side is misreconstructed by the same amount, resulting in a corresponding shift in the M_{BC} of each side by the same amount. Moreover, some of the candidates smeared along the diagonal are from continuum events. The remaining background events mainly come from candidates reconstructed incorrectly on both sides (BG-III). Here we list the PDFs for the corresponding components [30, 31] in the fit:

- Signal: $s(x, y)$,
- BG-I: $b(x) \cdot c_y(y; E_{\text{beam}}, \xi_y) + b(y) \cdot c_x(x; E_{\text{beam}}, \xi_x)$,
- BG-II: $c_z(z; \sqrt{2}E_{\text{beam}}, \xi_z) \cdot g(k; 0, \sigma_k)$,
- BG-III: $c_x(x; E_{\text{beam}}, \xi_x) \cdot c_y(y; E_{\text{beam}}, \xi_y)$.

Here, $x = M_{\text{BC}}^{\text{tag}}$, $y = M_{\text{BC}}^{\text{sig}}$, $z = (x + y)/\sqrt{2}$, and $k = (x - y)/\sqrt{2}$. The signal shape $s(x, y)$ is described by the 2D MC-simulated shape of $D^+ D^-$ convolved with two independent Gaussian functions. For BG-I, the function $b(x)$ is described by the one-dimensional (1D) MC-simulated shape of $D^+ (D^-)$ convolved with a Gaussian. The parameters of the Gaussian functions are obtained by a 1D fit to the M_{BC} distributions on the signal and tag side, and are fixed in the 2D fit. The BG-II fit component is given by an ARGUS function in the diagonal axis multiplied by a Gaussian in the anti-diagonal axis. The function $c_f(f; E_{\text{beam}}, \xi_f)$ is the ARGUS function [32] defined as

$$c_f(f; E_{\text{beam}}, \xi_f) = A_f f \left(1 - \frac{f^2}{E_{\text{beam}}^2}\right)^{\frac{1}{2}} e^{\xi_f \left(1 - \frac{f^2}{E_{\text{beam}}^2}\right)}, \quad (3)$$

where f denotes x, y or z , E_{beam} is fixed at 1.8865 GeV, A_f is a normalization factor, and ξ_f is a fit parameter. The function $g(k; \sigma_k)$ is a Gaussian distribution with a mean value of zero and a standard deviation $\sigma_k = \sigma_0 \cdot (\sqrt{2}E_{\text{beam}} - z)^p$, where σ_0 and p are parameters determined by the fit. The BG-III fit component is given by an ARGUS function in $M_{\text{BC}}^{\text{sig}}$ multiplied by an ARGUS function in $M_{\text{BC}}^{\text{tag}}$.

TABLE III. Yields obtained from the 2D fit. The uncertainties are statistical only.

$N_{K_S^0 \text{sig}}$	1296 ± 37
N_{sb1}	244 ± 16
N_{sb2}	11 ± 4
N_{net}	1177 ± 38

V. AMPLITUDE ANALYSIS

We perform a three-constraint kinematic fit to ensure that all the events lay within the phase space boundary, where the invariant masses of the signal D^+ and the two K_S^0 candidates are constrained to the corresponding known masses [25]. The updated four-momenta of the final state particles from the kinematic fit are used to perform the amplitude analysis. The amplitude analysis of $D^+ \rightarrow K_S^0 K_S^0 \pi^+$ is performed using an unbinned

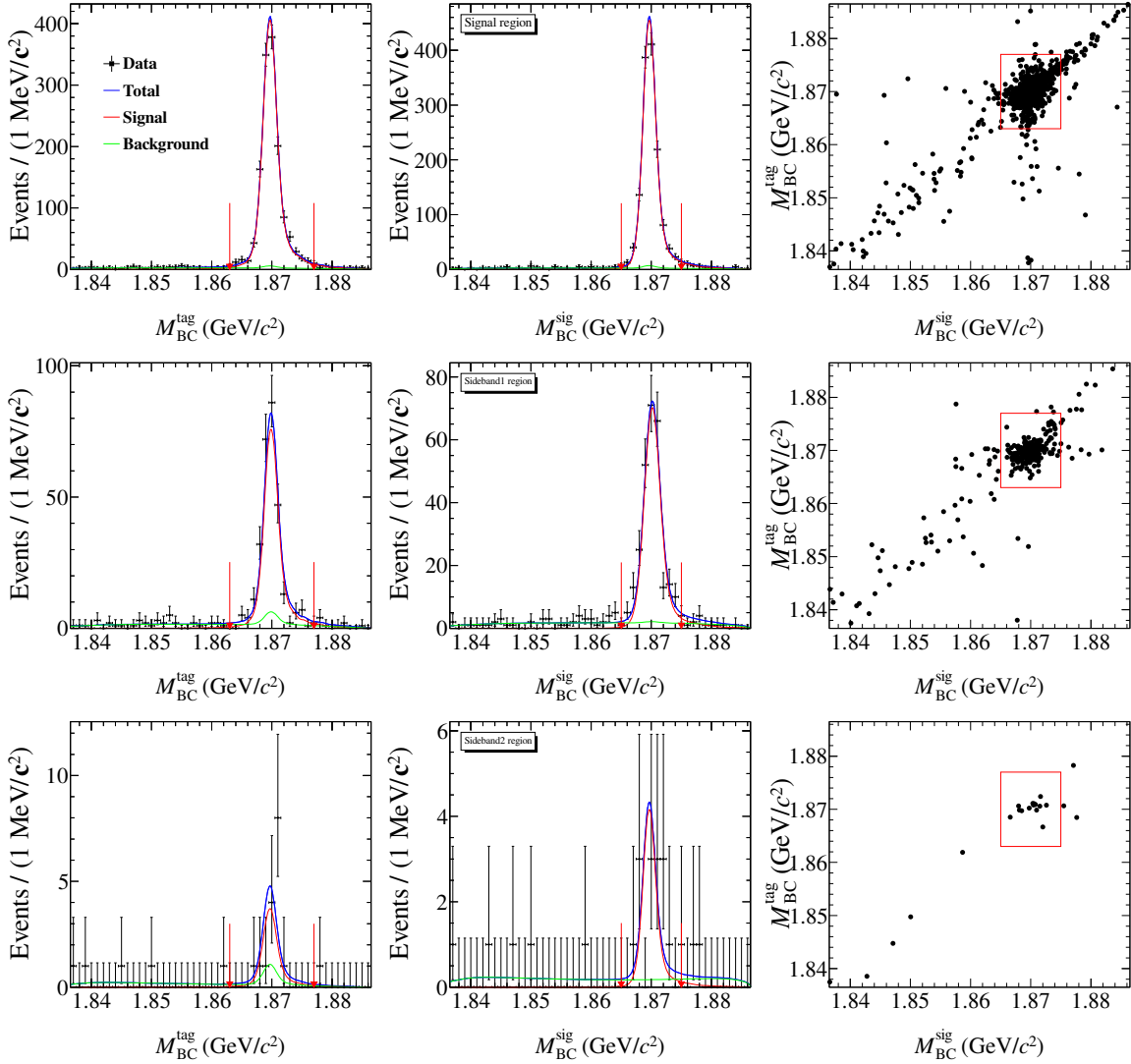


FIG. 3. Projections on M_{BC}^{tag} (left) and M_{BC}^{sig} (center) of the 2D fit. The black points with error bars are data, the blue lines are the total fit, the red lines are the signal shapes, the green lines are the sum of all backgrounds, and the pair of red arrows indicate the M_{BC} signal window. The right plots are the M_{BC}^{tag} versus M_{BC}^{sig} distributions, where the red box represents the signal region of M_{BC} . The first, second and third rows correspond to the fits to the candidate events in the signal region, the sideband 1 and the sideband 2 regions, respectively.

maximum likelihood fit. The likelihood function \mathcal{L} is constructed as

$$\ln \mathcal{L} = \sum_k^{N_{\text{data}}} \ln[\omega_{\text{sig}} f_S(p_j^k) + (1 - \omega_{\text{sig}}) f_B(p_j^k)], \quad (4)$$

where k indicates the k^{th} event in the data sample, N_{data} is the number of surviving events, p_j denotes the four-momenta of the j^{th} final state particles, f_S (f_B) is the signal (background) PDF and ω_{sig} is the signal purity of the DT events.

The signal PDF is given by

$$f_S(p_j) = \frac{\epsilon(p_j) |\mathcal{M}(p_j)|^2 R_3(p_j)}{\int \epsilon(p_j) |\mathcal{M}(p_j)|^2 R_3(p_j) dp_j}, \quad (5)$$

where $\epsilon(p)$ is the detection efficiency and $R_3(p)$ is the three-body phase space. Based on the isobar model, the total amplitude \mathcal{M} is constructed as the coherent sum of amplitudes of intermediate processes, given by $\mathcal{M}(p) = \sum c_n \mathcal{A}_n(p)$, where $c_n = \rho_n e^{i\phi_n}$ and $\mathcal{A}_n(p)$ are the complex coefficient and the amplitude for the n^{th} intermediate process, respectively. The magnitude ρ_n and phase ϕ_n are free parameters in the fit. The model is symmetrized with respect to the two identical K_S^0 mesons. We use covariant tensors to construct the amplitudes, which are written as

$$\mathcal{A}_n = P_n S_n F_n^r F_n^D, \quad (6)$$

where S_n is the spin factor [33], F_n^r and F_n^D are the Blatt-

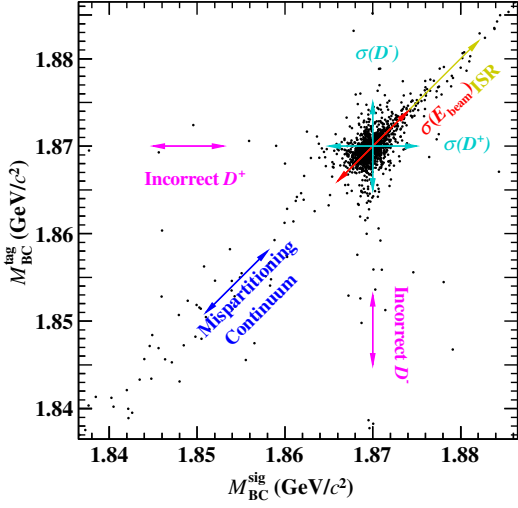


FIG. 4. Distribution of M_{BC}^{tag} versus M_{BC}^{sig} for the $D^+ \rightarrow K_S^0 K_S^0 \pi^+$ candidate events in data of K_S^0 signal region. The cyan arrows indicate the resolution caused by $D^{+(-)}$ momentum resolution ($\sigma(D^{+(-)})$), the red arrow by the beam energy spread ($\sigma(E_{\text{beam}})$), and the yellow arrow denotes the ISR effect. The pink and blue arrows indicate the background due to incorrectly reconstructed D^- or D^+ and mispartitioning continuum, respectively.

Weisskopf barrier factors of the intermediate state and the D^\pm meson decays [34], respectively, and P_n is the relativistic Breit-Wigner (RBW) function [35] describing the propagator of the intermediate resonance. The background PDF is given by

$$f_B(p_j) = \frac{B(p_j)R_3(p_j)}{\int \epsilon(p_j)B_\epsilon(p_j)R_3(p_j)dp_j}, \quad (7)$$

where $B_\epsilon(p_j) = B(p_j)/\epsilon(p_j)$ is the efficiency-corrected background shape, the $\epsilon(p_j)$ term is given by the number of selected events from the PHSP MC samples divided by the number of generated events in the $M_{K_S^0 K_S^0}^2$ versus $M_{K_S^0 \pi^+}^2$ 2D space. The shape of the background in data is modeled by the background events in the signal region derived from the inclusive MC samples. The invariant mass distributions of events outside the signal region show good agreement between data and MC simulation, thus validating the description from the inclusive MC samples. We have also examined the distributions of the background events of the inclusive MC samples inside and outside the signal region. Generally, they are consistent with each other within statistical uncertainties. The background shape $B(p)$ is modeled using a kernel estimation method [36] implemented in RooFit [37] to model the distribution of an input dataset as a superposition of Gaussian kernels. The normalization integrals in the denominators are calculated by the phase space

MC sample, which are

$$\int \epsilon |\mathcal{M}(p_j)|^2 R_3 dp_j \propto \frac{1}{N_{\text{MC}}} \sum_{k_{\text{MC}}}^{N_{\text{MC}}} \frac{|\mathcal{M}(p_j^{k_{\text{MC}}})|^2}{|\mathcal{M}^{\text{gen}}(p_j^{k_{\text{MC}}})|^2}, \quad (8)$$

$$\int \epsilon B_\epsilon(p_j) R_3 dp_j \propto \frac{1}{N_{\text{MC}}} \sum_{k_{\text{MC}}}^{N_{\text{MC}}} \frac{B_\epsilon(p_j^{k_{\text{MC}}})}{|\mathcal{M}^{\text{gen}}(p_j^{k_{\text{MC}}})|^2}, \quad (9)$$

where k_{MC} is the index of the k^{th} event of the MC sample and N_{MC} is the number of selected MC events. The $\mathcal{M}^{\text{gen}}(p_j)$ is the signal PDF used to generate the MC samples in MC integration.

Tracking, PID and K_S^0 reconstruction efficiency differences between data and MC simulation are corrected by multiplying the MC events by a correction factor γ_ϵ , which is calculated as

$$\gamma_\epsilon(p_j) = \prod_n \frac{\epsilon_{n,\text{data}}(p_j)}{\epsilon_{n,\text{MC}}(p_j)}, \quad (10)$$

where n refers to tracking, PID or K_S^0 reconstruction, and $\epsilon_{n,\text{data}}(p_j)$ and $\epsilon_{n,\text{MC}}(p_j)$ are their efficiencies as a function of the momenta of the daughter particles for data and MC simulation, respectively. The specific values of these efficiencies are obtained using different control samples. More detailed information can be found in section 7, as part of the uncertainty studies for the BF measurement. By weighting each MC event with γ_ϵ , the MC integration is modified to be

$$\int \epsilon |\mathcal{M}(p_j)|^2 R_3 dp_j \propto \frac{1}{N_{\text{MC}}} \sum_{k_{\text{MC}}}^{N_{\text{MC}}} \frac{\gamma_\epsilon |\mathcal{M}(p_j^{k_{\text{MC}}})|^2}{|\mathcal{M}^{\text{gen}}(p_j^{k_{\text{MC}}})|^2}, \quad (11)$$

$$\int \epsilon B_\epsilon R_3 dp_j \propto \frac{1}{N_{\text{MC}}} \sum_{k_{\text{MC}}}^{N_{\text{MC}}} \frac{\gamma_\epsilon B_\epsilon(p_j^{k_{\text{MC}}})}{|\mathcal{M}^{\text{gen}}(p_j^{k_{\text{MC}}})|^2}. \quad (12)$$

For a decay process $a \rightarrow b c$, the Blatt-Weisskopf barrier factors [34] depend on the angular momentum L and the momentum q of the final-state particle b or c in the rest system of a . They are taken as

$$\begin{aligned} F_{L=0}(q) &= 1, \\ F_{L=1}(q) &= \sqrt{\frac{z_0^2 + 1}{z^2 + 1}}, \\ F_{L=2}(q) &= \sqrt{\frac{z_0^4 + 3z_0^2 + 9}{z^4 + 3z^2 + 9}}, \end{aligned} \quad (13)$$

where $z = qR$ and $z_0 = q_0R$. The effective radius of barrier R is fixed to be 3.0 (GeV/c)^{-1} for the intermediate resonances and 5.0 (GeV/c)^{-1} for the D^+ meson. The momentum q is given by

$$q = \sqrt{\frac{(s_a + s_b - s_c)^2}{4s_a} - s_b}, \quad (14)$$

where s_a, s_b , and s_c are the invariant mass squared of particles a , b and c , respectively. The value of q_0 is that of q when $s_a = m_a^2$, where m_a is the mass of particle a .

The intermediate resonances $K^*(892)^+, K_2^*(1430)^+, f_0(1370), a_0(1450)^0, K_0^*(1680)^+$ are parameterized with the RBW formulas,

$$P(m) = \frac{1}{m_0^2 - m^2 - im_0\Gamma(m)}, \quad (15)$$

$$\Gamma(m) = \Gamma_0 \left(\frac{q}{q_0}\right)^{2L+1} \left(\frac{m_0}{m}\right) \left(\frac{F_L(q)}{F_L(q_0)}\right)^2,$$

where m is the invariant mass of the decay products, and m_0 and Γ_0 are the rest mass and width of the intermediate resonance, which are fixed to their known values [25]. The energy-dependent width is denoted by $\Gamma(m)$.

The $K\pi$ \mathcal{S} -wave modeled by the LASS parameterization [38] is described by a $K_0^*(1430)$ Breit-Wigner together with an effective range non-resonant component with a phase shift, given by

$$A(m) = F\sin\delta_F e^{i\delta_F} + R\sin\delta_R e^{i\delta_R} e^{i2\delta_F}, \quad (16)$$

with

$$\delta_F = \phi_F + \cot^{-1} \left[\frac{1}{aq} + \frac{rq}{2} \right], \quad (17)$$

$$\delta_R = \phi_R + \tan^{-1} \left[\frac{M\Gamma(m_{K\pi})}{M^2 - m_{K\pi}^2} \right],$$

where the parameters F (ϕ_F) and R (ϕ_R) are the magnitudes (phases) for the non-resonant state and resonance terms, respectively. The parameters a and r are the scattering length and effective interaction length, respectively. M and Γ are the BW parameters of the $K_0^*(1430)$. We fix these parameters ($M, \Gamma, F, \phi_F, R, \phi_R, a, r$) to the *BABAR* and *Belle* results [39]. These parameters are summarized in Table IV.

TABLE IV. The $K\pi$ \mathcal{S} -wave parameters, obtained from the fit to the $D^0 \rightarrow K_S^0\pi^+\pi^-$ Dalitz plot distribution in the *BABAR* and *Belle* experiments [39]. Uncertainties are statistical only.

M (GeV/ c^2)	1.441 ± 0.002
Γ (GeV)	0.193 ± 0.004
F	0.96 ± 0.07
ϕ_F ($^\circ$)	0.1 ± 0.3
R	1(fixed)
ϕ_R ($^\circ$)	-109.7 ± 2.6
a (GeV/ c^2)	0.113 ± 0.006
r (GeV/ c^2)	-33.8 ± 1.8

The $f_0(980)$ is parameterized with the Flatté formula [40]:

$$P_{f_0(980)} = \frac{1}{M_{f_0(980)}^2 - m^2 - i(g_{\pi\pi}\rho_{\pi\pi}(m^2) + g_{K\bar{K}}\rho_{K\bar{K}}(m^2))}, \quad (18)$$

where $g_{\pi\pi, K\bar{K}}$ are the coupling constants to individual final states. The parameters are fixed to be $g_{\pi\pi} = (0.165 \pm 0.010 \pm 0.015)\text{GeV}^2/c^4$, $g_{K\bar{K}} = (4.21 \pm 0.25 \pm 0.21)g_{\pi\pi}$ and $M = 0.965 \text{ GeV}/c^2$, as reported in Ref. [40]. The Lorentz invariant phase space factors $\rho_{\pi\pi}(s)$ and $\rho_{K\bar{K}}(s)$ are given by

$$\rho_{\pi\pi} = \frac{2}{3} \sqrt{1 - \frac{4m_{\pi^\pm}^2}{m^2}} + \frac{1}{3} \sqrt{1 - \frac{4m_{\pi^0}^2}{m^2}}, \quad (19)$$

$$\rho_{K\bar{K}} = \frac{1}{2} \sqrt{1 - \frac{4m_{K^\pm}^2}{m^2}} + \frac{1}{2} \sqrt{1 - \frac{4m_{K^0}^2}{m^2}}.$$

Figure 5(a) shows the Dalitz plot of $M_{K_S^0(1)\pi^+}$ versus $M_{K_S^0(2)\pi^+}$ of the selected DT candidates from the data samples, where $K_S^0(1)$ and $K_S^0(2)$ are randomly selected from two indistinguishable K_S^0 candidates. The vertical and horizontal bands around $0.8 \text{ GeV}^2/c^4$ indicate the decay $D^+ \rightarrow K_S^0 K^*(892)^+$. We choose this process as a reference so that magnitudes and phases of other amplitudes are defined relative to it. Other possible contributions from the resonances such as $f_0(980), f_0(1370), K_2^*(1430)^+, a_0(1450)^0, K_0^*(1680)^+$ and $K\pi$ \mathcal{S} -wave are added to the fit one at a time. The statistical significance of each resonance is calculated from the change of the log-likelihood taking the variation in the number of degrees of freedom into account. Different combinations of these resonances are also tested. In addition to the reference amplitude $D^+ \rightarrow K_S^0 K^*(892)^+$, the amplitude for $D^+ \rightarrow K_S^0 (K_S^0 \pi^+)_{\mathcal{S}\text{-wave}}$ is found to have a significance larger than 10σ . No other contribution has a significance larger than 3σ . The significance of the $f_0(980)$ contribution is less than 1σ . The Dalitz plot of the signal MC sample generated based on the result of the amplitude analysis is shown in Fig. 5(b). The mass projections of the fit are shown in Fig. 6. The fit quality is determined as $\chi^2/\text{NDF} = 113.1/125$ using an adaptive binning of the $M_{K_S^0 K_S^0}^2$ versus $M_{K_S^0 \pi^+}$, where the Dalitz plot that each bin requires must contain at least 10 events.

The contribution of the n^{th} amplitude relative to the total BF is quantified by the fit fraction (FF) defined as $\text{FF}_n = \int |\rho_n A_n|^2 dR_3 / \int |\mathcal{M}|^2 dR_3$. The FFs and the phase difference relative to the reference process are listed in Table V. The sum of the two FFs is 102.2%. The sum of these FFs is generally not unity due to net constructive or destructive interference.

VI. SYSTEMATIC UNCERTAINTY OF THE AMPLITUDE ANALYSIS

The systematic uncertainties for the amplitude analysis results, including the phase and FFs, can be categorized into the following sources: (I) input parameters, (II)

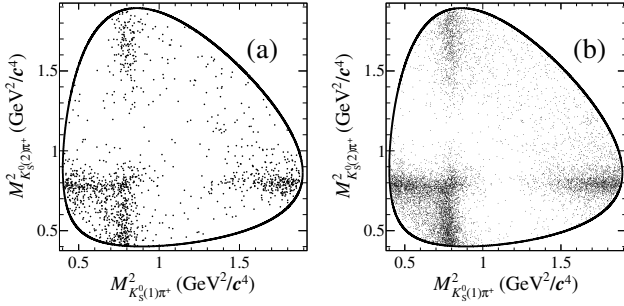


FIG. 5. Dalitz plots of $M_{K_S^0(1)\pi^+}^2$ versus $M_{K_S^0(2)\pi^+}^2$ for $D^+ \rightarrow K_S^0 K_S^0 \pi^+$, $K_S^0(1)$ and $K_S^0(2)$ are randomly selected from two indistinguishable K_S^0 candidates, of (a) the sum of all data samples and (b) the signal MC samples generated based on the amplitude analysis result. The black curves indicate the kinematic boundary.

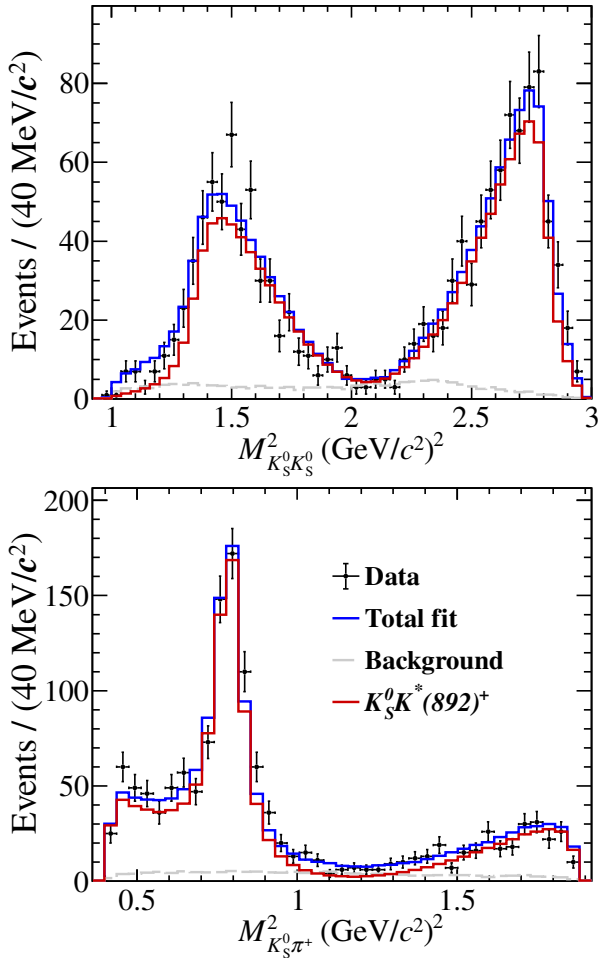


FIG. 6. Distributions of $M_{K_S^0 K_S^0}^2$ and $M_{K_S^0 \pi^+}^2$ from the nominal fit. The $M_{K_S^0 \pi^+}^2$ distribution only contains one $K_S^0 \pi^+$ combination, in which K_S^0 is labelled randomly due to the indistinguishable K_S^0 candidates. The points with error bars are data and the blue lines are the total fit result. The red solid lines are the $D^+ \rightarrow K_S^0 K^*(892)^+$ component. The dashed grey lines are the simulated background derived from the inclusive MC sample.

TABLE V. The obtained FFs and phase difference to the reference amplitude. The first and the second uncertainties are statistical and systematic, respectively.

Amplitude	Phase	FF (%)
$D^+ \rightarrow K_S^0 K^*(892)^+$	0.0(fixed)	$97.8 \pm 1.0 \pm 0.3$
$D^+ \rightarrow K_S^0 (K_S^0 \pi^+)_{S\text{-wave}}$	$1.4 \pm 0.2 \pm 0.1$	$4.4 \pm 1.0 \pm 0.2$

radii of the mesons, (III) background, (IV) efficiency, (V) fit bias. For each kind of source, the related parameters are varied and the results of the new fit are compared to the results of the nominal fit, considering the difference as the corresponding uncertainty. The results of the systematic uncertainties for phase and FFs are summarized in Table VI, where the uncertainties are given in units of the corresponding statistical uncertainties. The total uncertainties are obtained by adding these contributions in quadrature.

TABLE VI. Systematic uncertainties on the phase ϕ and FFs for different amplitudes in units of the corresponding statistical uncertainties. (I) input parameters, (II) radii of the mesons, (III) background, (IV) efficiency, (V) fit bias. The total systematic uncertainties are obtained by summing up all contributions in quadrature.

Source	$D^+ \rightarrow K_S^0 K^*(892)^+$	$D^+ \rightarrow K_S^0 (K_S^0 \pi^+)_{S\text{-wave}}$	
	FF	Phase ϕ	FF
I	0.12	0.15	0.06
II	0.12	0.14	0.06
III	0.13	0.12	0.10
IV	0.04	0.40	0.13
V	0.07	0.06	0.08
Total	0.23	0.47	0.20

(I) *Input parameters*: in the nominal fit, mass and width of the $K^*(892)^+$ are fixed to the values from PDG [25]. The parameters of the LASS model are fixed according to Ref. [39]. To estimate the corresponding systematic uncertainties, the fit procedure is repeated by varying one by one each of the fixed parameters by $\pm 1\sigma$. The quadratic sum of the largest relative variations for each parameter is taken as the systematic uncertainty.

(II) *Radii of the mesons*: the radii of the Blatt-Weisskopf barrier factors are varied from their nominal values of 5 GeV^{-1} and 3 GeV^{-1} (for the D^+ meson and the intermediate resonances, respectively) by $\pm 1 \text{ GeV}^{-1}$.

(III) *Background*: the uncertainties from the background size is studied by varying the signal fraction (equivalent to the fraction of background), i.e. ω_{sig} in Eq. (4), by $\pm 1\sigma$. Another source of systematic uncertainty comes from the modelization of the background shape, which is estimated by varying the parameter of RooNDKeysPDF describing the smoothness of the shape

from 1.5 to 2 or 1, and extracting the shape with two different variables ($M_{K_S^0 K_S^0}^2$ and $M_{K_S^0 \pi^+}^2$). The largest difference from the nominal results is considered as the uncertainty.

(IV) *Efficiency*: the systematic uncertainty from the γ_ϵ factor in Eq. (10), which corrects for data-MC differences in tracking, PID and K_S^0 reconstruction efficiencies, is evaluated by performing the fit after varying the γ_ϵ factor by $\pm 1\sigma$.

Tracking and PID efficiencies of π^+ are studied by the control samples of $D^0 \rightarrow K^-\pi^+$, $D^0 \rightarrow K^-\pi^+\pi^0$, $D^0 \rightarrow K^-\pi^+\pi^+\pi^-$ versus $\bar{D}^0 \rightarrow K^+\pi^-$, $\bar{D}^0 \rightarrow K^+\pi^-\pi^0$, $\bar{D}^0 \rightarrow K^+\pi^-\pi^-\pi^+$ and $D^+ \rightarrow K^-\pi^+\pi^+$ versus $D^- \rightarrow K^+\pi^-\pi^-$. The K_S^0 reconstruction efficiency is studied by the control samples from $\psi(3770) \rightarrow D^0\bar{D}^0/D^+D^-$ and selected by DT method. The tag modes are $\bar{D}^0 \rightarrow K^-\pi^+$, $\bar{D}^0 \rightarrow K^-\pi^+\pi^0$, $\bar{D}^0 \rightarrow K^-\pi^+\pi^+\pi^-$, $D^- \rightarrow K^+\pi^-\pi^-$ and the signal modes are: $D^0 \rightarrow K_S^0\pi^+\pi^-$, $D^0 \rightarrow K_S^0\pi^+\pi^-\pi^0$, $D^0 \rightarrow K_S^0\pi^0$, $D^+ \rightarrow K_S^0\pi^+$, $D^+ \rightarrow K_S^0\pi^+\pi^0$, $D^+ \rightarrow K_S^0\pi^+\pi^+\pi^-$.

(V) *Fit bias*: to study the possible bias from the fit procedure, an ensemble of 300 signal MC samples is generated according to the results of the amplitude analysis. The fit procedure is repeated for each signal MC sample, and the pull distributions of the amplitude results are fitted by a Gaussian. The obtained mean values are assigned as the correlated systematic uncertainty.

VII. BRANCHING FRACTION MEASUREMENT

The BF of $D^+ \rightarrow K_S^0 K_S^0 \pi^+$ is measured with the DT technique using the same tag modes and event selection criteria as the ones in the amplitude analysis. The BF is given by

$$\mathcal{B}_{\text{sig}} = \frac{N_{\text{net}}}{\sum_{\alpha} N_{\alpha}^{\text{ST}} \epsilon_{\alpha}^{\text{DT}} / \epsilon_{\alpha}^{\text{ST}}}, \quad (20)$$

where α runs over the various tag modes. The DT efficiency ($\epsilon_{\alpha}^{\text{DT}}$) is the signal selection efficiency for an event with a D^- in the α -th tag mode. The ST yields (N_{α}^{ST}) and ST efficiencies ($\epsilon_{\alpha}^{\text{ST}}$) for each tag mode are obtained by fitting the corresponding $M_{\text{BC}}^{\text{tag}}$ distributions individually. The corresponding $\epsilon_{\alpha}^{\text{DT}}$, N_{α}^{ST} and $\epsilon_{\alpha}^{\text{ST}}$ are summarized in Table VII. The DT yield N_{net} is listed in Table III. In the fits to the $M_{\text{BC}}^{\text{tag}}$ distributions, the signal shape is modeled with the MC-simulated shape convolved with a double-Gaussian function. The background is parameterized as an ARGUS function [32] with an endpoint parameter fixed at 1.8865 GeV/ c^2 . Figure 7 shows the fit results. The candidates with $M_{\text{BC}}^{\text{tag}}$ within (1.863, 1.877)

GeV/ c^2 for each tag mode are kept for further analysis. The corresponding DT efficiencies $\epsilon_{\alpha, \text{sig}}^{\text{DT}}$ are obtained by analyzing the signal MC samples, with the signal events for $D^+ \rightarrow K_S^0 K_S^0 \pi^+$ generated based on the results of the amplitude analysis. After correcting for the differences in π^{\pm} tracking, PID and K_S^0 reconstruction efficiencies between data and MC simulation, we determine the BF to be $(2.97 \pm 0.09_{\text{stat.}} \pm 0.05_{\text{syst.}}) \times 10^{-3}$. The systematic uncertainty will be discussed in the following section.

TABLE VII. The ST yields (N_{α}^{ST}), ST efficiencies ($\epsilon_{\alpha}^{\text{ST}}$) and DT efficiencies ($\epsilon_{\alpha}^{\text{DT}}$) for six tag modes. The BFs of the sub-particle (K_S^0, π^0) decays are not included. The uncertainties are statistical only.

Tag mode α	N_{α}^{ST}	$\epsilon_{\alpha}^{\text{ST}}(\%)$	$\epsilon_{\alpha}^{\text{DT}}(\%)$
$K^+\pi^-\pi^-$	2164074 ± 1571	51.17 ± 0.01	11.00 ± 0.01
$K^+\pi^-\pi^-\pi^0$	689042 ± 1172	25.50 ± 0.01	4.83 ± 0.01
$K_S^0\pi^-$	250437 ± 524	50.63 ± 0.02	10.83 ± 0.02
$K_S^0\pi^-\pi^0$	558495 ± 930	26.28 ± 0.01	4.98 ± 0.01
$K_S^0\pi^-\pi^-\pi^+$	300519 ± 669	28.97 ± 0.01	4.94 ± 0.01
$K^+K^-\pi^-$	187379 ± 541	41.06 ± 0.02	8.75 ± 0.02

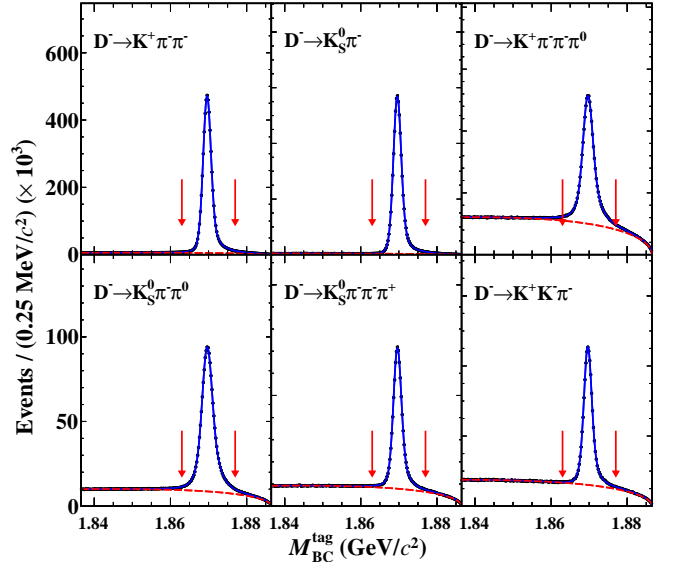


FIG. 7. Fits to the $M_{\text{BC}}^{\text{tag}}$ distributions of the ST D^- candidates. The data samples are represented by points with error bars, the total fit results by solid blue lines and the red dashed curves describe the fitted combinatorial background shapes. The pair of red arrows indicate the M_{BC} signal window.

VIII. SYSTEMATIC UNCERTAINTY OF BF MEASUREMENT

Most systematic uncertainties related to the efficiency of reconstructing the D^{\pm} mesons on the tag side are can-

celed due to the DT method. The following sources are taken into consideration to evaluate the systematic uncertainties in the BF measurement. The total systematic uncertainties are summarized in Table VIII. Adding them in quadrature results in a total systematic uncertainty of 1.6% in the BF measurement.

(I) *ST D^- yield*: the systematic uncertainty in the ST yield has been estimated by varying the signal and background shapes in the fit. This systematic uncertainty is assigned to be 0.1%.

(II) *Tracking and PID efficiencies*: the data-MC efficiency ratios for π^- tracking and PID efficiencies are determined to be 0.998 ± 0.001 and 0.998 ± 0.001 for this decay channel by using the same control samples used for the amplitude analysis uncertainties. After correcting the MC efficiencies to data by these factors, the statistical uncertainties of the correction parameters are assigned as the systematic uncertainties, which are 0.1% for both π^\pm PID and tracking.

(III) *2D fit*: the uncertainty associated with the signal and background shapes in the 2D fit to the DT M_{BC} distribution is 1.1%, determined by varying the mean value and the resolution of the smeared Gaussian function by $\pm 1\sigma$ and varying the ARGUS end-point by $\pm 0.2 \text{ MeV}/c^2$.

(IV) *K_S^0 reconstruction*: the data-MC efficiency ratio for K_S^0 reconstruction is determined to be 0.990 ± 0.004 by using the same control samples used for the amplitude analysis uncertainties. After correcting the efficiency by this factor for the two K_S^0 mesons, we assign 0.8% as the systematic uncertainty from the reconstruction of each K_S^0 .

(V) *Amplitude model*: the uncertainty from the signal MC model based on the results of the amplitude analysis is studied by varying the fit parameters according to the covariance matrix. The change of signal efficiency is estimated to be 0.2%.

(VI) *Peaking background estimation*: according to the Eq. (2), in the nominal analysis, the normalization factor for the peaking backgrounds (i.e. the ratio of the background yields between the K_S^0 signal and the sideband 1 regions) is assumed to be 0.5. The BF is recalculated with alternative normalization factors determined by MC simulation. The corresponding change on the BF, 0.7% for $D^+ \rightarrow K_S^0 K_S^0 \pi^+$, is assigned as the systematic uncertainty associated with the peaking background normalization. We have also examined the contributions of the sideband 2 region, but since the effects on the net number of events are negligible, we ignore them in this work.

(VII) *Quoted \mathcal{B}* : in this measurement, the BF of $K_S^0 \rightarrow \pi^+ \pi^-$ is quoted from the PDG [25], which is $\mathcal{B}(K_S^0 \rightarrow \pi^+ \pi^-) = (69.20 \pm 0.05)\%$. The associated uncertainty is assigned to be 0.1%.

(VIII) *ΔE requirement*: considering the possible difference between data and MC simulation, we examine the ΔE_{sig} cut efficiency after smearing a double-Gaussian function for signal MC sample, and we take the change of this efficiency, 0.5%, as the systematic uncertainty.

TABLE VIII. Systematic uncertainties for the BF measurement.

Source	Uncertainty (%)
ST D^- yield	0.1
PID efficiency	0.1
Tracking efficiency	0.1
2D fit	1.1
K_S^0 reconstruction	0.8
Amplitude model	0.2
Peaking background estimation	0.7
Quoted \mathcal{B}	0.1
ΔE requirement	0.5
Total	1.6

IX. SUMMARY

Based on e^+e^- collision data corresponding to an integrated luminosity of 7.93 fb^{-1} collected with the BESIII detector at the center-of-mass energy 3.773 GeV , the first amplitude analysis of the decay $D^+ \rightarrow K_S^0 K_S^0 \pi^+$ is performed. The fit results are listed in Table V. In addition, with the detection efficiency obtained from the signal MC sample generated based on the amplitude analysis results, we obtain the BF $\mathcal{B}(D^+ \rightarrow K_S^0 K_S^0 \pi^+) = (2.97 \pm 0.09_{\text{stat.}} \pm 0.05_{\text{syst.}}) \times 10^{-3}$. The BF for $D^+ \rightarrow K_S^0 K^*(892)^+ \rightarrow K_S^0 \pi^+$ is calculated as $\text{FF} \times \mathcal{B}(D^+ \rightarrow K_S^0 K_S^0 \pi^+) / \mathcal{B}(K^*(892)^+ \rightarrow K_S^0 \pi^+)$ to be $\mathcal{B}(D^+ \rightarrow K_S^0 K^*(892)^+) = (8.72 \pm 0.28_{\text{stat.}} \pm 0.15_{\text{syst.}}) \times 10^{-3}$, which is consistent with the previous BESIII measurement [9] but with improved precision.

Compared to the theoretical expectations of Table I, this result deviates from those in Refs. [2, 11] by more than five standard deviations, while is consistent with that based on the theoretical expectations [10, 12] within two standard deviations and the predictions in Ref. [1] within three standard deviations.

ACKNOWLEDGEMENT

The BESIII Collaboration thanks the staff of BEPCII and the IHEP computing center for their strong support. This work is supported in part by National Key R&D Program of China under Contracts Nos. 2023YFA1606000, 2020YFA0406400, 2020YFA0406300; National Natural Science Foundation of China (NSFC) under Contracts Nos. 11635010, 11735014, 11935015,

11935016, 11935018, 12025502, 12035009, 12035013, 12061131003, 12192260, 12192261, 12192262, 12192263, 12192264, 12192265, 12221005, 12225509, 12235017, 12361141819, 12375087, 18175054; the Chinese Academy of Sciences (CAS) Large-Scale Scientific Facility Program; the CAS Center for Excellence in Particle Physics (CCEPP); Joint Large-Scale Scientific Facility Funds of the NSFC and CAS under Contract No. U1832207, U2032104; the Excellent Youth Foundation of Henan Scientific Committee under Contract No. 242300421044; 100 Talents Program of CAS; The Institute of Nuclear and Particle Physics (INPAC) and Shanghai Key Laboratory for Particle Physics and Cosmology; German Research Foundation DFG under Contracts Nos. 455635585, FOR5327, GRK 2149; Istituto Nazionale di Fisica Nucleare, Italy; Ministry of Development of Turkey under Contract No. DPT2006K-120470; National Research Foundation of Korea under Contract No. NRF-2022R1A2C1092335; National Science and Technology fund of Mongolia; National Science Research and Innovation Fund (NSRF) via the Program Management Unit for Human Resources & Institutional Development, Research and Innovation of Thailand under Contract No. B16F640076; Polish National Science Centre under Contract No. 2019/35/O/ST2/02907; The Swedish Research Council; U. S. Department of Energy under Contract No. DE-FG02-05ER41374.

[1] H. Y. Cheng, C. W. Chiang and A. L. Kuo, *Phys. Rev. D* **93**, 114010 (2016).
 [2] H. Y. Cheng and C. W. Chiang, *Phys. Rev. D* **100**, 093002 (2019).
 [3] H. Y. Cheng and C. W. Chiang, *Phys. Rev. D* **81**, 074021 (2010).
 [4] Y. K. Hsiao, Y. Yu, and B. C. Ke, *Eur. Phys. J. C* **80**, 895 (2020).
 [5] Y. Yu, Y. K. Hsiao, and B. C. Ke, *Eur. Phys. J. C* **81**, 1093 (2021).
 [6] Y. K. Hsiao, S. Q. Yang, W. J. Wei, and B. C. Ke, [arXiv:2306.06091 \[hep-ph\]](https://arxiv.org/abs/2306.06091).
 [7] Y. Cao, Y. Cheng and Q. Zhao, *Phys. Rev. D* **109**, 073002 (2024).
 [8] M. Ablikim *et al.* (BESIII Collaboration), *Phys. Rev. D* **99**, 032002 (2019).
 [9] M. Ablikim *et al.* (BESIII Collaboration), *Phys. Rev. D* **104**, 012006 (2021).
 [10] F. S. Yu, X. X. Wang and C. D. Lyu, *Phys. Rev. D* **84**, 074019 (2011).
 [11] Q. Qin, H. N. Li, C. D. Lyu and F. S. Yu, *Phys. Rev. D* **89**, 054006 (2014).
 [12] H. Y. Cheng and C. W. Chiang, *Phys. Rev. D* **109**, 073008 (2024).

[13] M. Ablikim *et al.* (BESIII Collaboration), *Phys. Lett. B* **765**, 231 (2017).
 [14] M. Ablikim *et al.* (BESIII Collaboration), [arXiv:2406.05827](https://arxiv.org/abs/2406.05827).
 [15] M. Ablikim *et al.* (BESIII Collaboration), *Nucl. Instrum. Methods Phys. Res. Sect. A* **614**, 345 (2010).
 [16] C. H. Yu *et al.*, *Proceedings of IPAC2016*, Busan, Korea, 2016.
 [17] M. Ablikim *et al.* (BESIII Collaboration), *Chin. Phys. C* **44**, 040001 (2020).
 [18] J. Lu, Y. Xiao, and X. Ji, *Radiat. Detect. Technol. Methods* **4**, 337 (2020).
 [19] J. W. Zhang *et al.*, *Radiat. Detect. Technol. Methods* **6**, 289 (2022).
 [20] X. Li *et al.*, *Radiat. Detect. Technol. Methods* **1**, 13 (2017); Y. X. Guo *et al.*, *Radiat. Detect. Technol. Methods* **1**, 15 (2017); P. Cao *et al.*, *Nucl. Instrum. Meth. A* **953**, 163053 (2020).
 [21] S. Agostinelli *et al.* (GEANT4 Collaboration), *Nucl. Instrum. Meth. A* **506**, 250 (2003).
 [22] K. X. Huang *et al.*, *Nucl. Sci. Tech.* **33**, 142 (2022).
 [23] S. Jadach, B. F. L. Ward, and Z. Was, *Phys. Rev. D* **63**, 113009 (2001); *Comput. Phys. Commun.* **130**, 260 (2000).
 [24] D. J. Lange, *Nucl. Instrum. Meth. A* **462**, 152 (2001); R. G. Ping, *Chin. Phys. C* **32**, 599 (2008).
 [25] R. L. Workman *et al.* (Particle Data Group), *Prog. Theor. Exp. Phys.* **2022**, 083C01 (2022).
 [26] J. C. Chen, G. S. Huang, X. R. Qi, D. H. Zhang, and Y. S. Zhu, *Phys. Rev. D* **62**, 034003 (2000); R. L. Yang, R. G. Ping and H. Chen, *Chin. Phys. Lett.* **31**, 061301 (2014).
 [27] E. Richter-Was, *Phys. Lett. B* **303**, 163 (1993).
 [28] J. Adler *et al.* (MARK-III Collaboration), *Phys. Rev. Lett.* **62**, 1821 (1989).
 [29] B. C. Ke, J. Koponen, H. B. Li and Y. Zheng, *Ann. Rev. Nucl. Part. Sci.* **73**, 285-314 (2023).
 [30] M. Ablikim *et al.* (BESIII Collaboration), *Phys. Rev. D* **101**, 052009 (2020).
 [31] M. Artuso *et al.* (CLEO Collaboration), *Phys. Rev. D* **76**, 112001 (2007).
 [32] H. Albrecht *et al.* (ARGUS Collaboration), *Phys. Lett. B* **241**, 278 (1990).
 [33] B. S. Zou and D. V. Bugg, *Eur. Phys. J. A* **16**, 537 (2003).
 [34] J. M. Blatt and V. F. Weisskopf, *Theoretical Nuclear Physics* (John Wiley & Sons, New York, 1973).
 [35] J. D. Jackson, *N. Cimento* **34**, 1644 (1964).
 [36] K. Cranmer, *Comput. Phys. Commun.* **136**, 198 (2001).
 [37] W. Verkerke and D. P. Kirkby, *RooFit Users Manual v2.91* (2019).
 [38] D. Aston *et al.*, *Nucl. Phys.* **B296**, 493 (1988).
 [39] I. Adachi *et al.* (BABAR and Belle Collaborations), *Phys. Rev. D* **98**, 112012 (2018).
 [40] M. Ablikim *et al.* (BESIII Collaboration), *Phys. Lett. B* **607**, 243 (2005).